

Chandra X-ray Observations of Two Unusual BAL Quasars

Jesse A. Rogerson^a, Patrick B. Hall^a, Stephanie A. Snedden^b, Michael S. Brotherton^c, Scott F. Anderson^d

^aDepartment of Physics and Astronomy, York University, Toronto, Ontario M3J 1P3, Canada

^bApache Point Observatory, P.O. Box 59, Sunspot, NM 88349-0059

^cDepartment of Physics and Astronomy, University of Wyoming, Laramie, WY 82071

^dUniversity of Washington, Department of Astronomy, Seattle, WA 98195

Abstract

We report sensitive *Chandra* X-ray non-detections of two unusual, luminous Iron Low-Ionization Broad Absorption Line Quasars (FeLoBALs). The observations do detect a non-BAL, wide-binary companion quasar to one of the FeLoBAL quasars. We combine X-ray-derived column density lower limits (assuming solar metallicity) with column densities measured from ultraviolet spectra and CLOUDY photoionization simulations to explore whether constant-density slabs at broad-line region densities can match the physical parameters of these two BAL outflows, and find that they cannot. In the “overlapping-trough” object SDSS J0300+0048, we measure the column density of the X-ray absorbing gas to be $N_H \geq 1.8 \times 10^{24} \text{ cm}^{-2}$. From the presence of Fe II UV78 absorption but lack of Fe II UV195/UV196 absorption, we infer the density in that part of the absorbing region to be $n_e \approx 10^6 \text{ cm}^{-3}$. We do find that a slab of gas at that density might be able to explain this object’s absorption. In the Fe III-dominant object SDSS J2215–0045, the X-ray absorbing column density of $N_H \geq 3.4 \times 10^{24} \text{ cm}^{-2}$ is consistent with the Fe III-derived $N_H \geq 2 \times 10^{22} \text{ cm}^{-2}$ provided the ionization parameter is $\log U > 1.0$ for both the $n_e = 10^{11} \text{ cm}^{-3}$ and $n_e = 10^{12} \text{ cm}^{-3}$ scenarios considered (such densities are required to produce Fe III absorption without Fe II absorption). However, the velocity width of the absorption rules out its being concentrated in a single slab at these densities. Instead, this object’s spectrum can be explained by a low density, high ionization and high temperature disk wind that encounters and ablates higher density, lower ionization Fe III-emitting clumps.

Keywords: quasars: general, absorption lines, individual (SDSS J030000.56+004828.0, SDSS J221511.94–004549.9, SDSS J025959.68+004813.6)

1. Introduction

Broad Absorption Line (BAL) quasar spectra are not as common as typical quasar spectra but provide a unique look at the central regions of Active Galactic Nuclei (AGN). A BAL quasar is characterized by absorption troughs from gas with blueshifted outflow velocities of typically 10% the speed of light ($0.1c$) (Weymann et al. 1991). The lower limit on the width of a BAL trough is in part a matter of definition; the traditional required minimum width is 2000 km s^{-1} (Weymann et al. 1991), but a minimum width of 1000 km s^{-1} has also been used (Trump et al. 2006). Such velocity widths are larger than essentially all galactic wind outflows, and thus ensure a sample of outflows driven predominantly by AGN; of course, narrower AGN-driven outflows can and do exist.

Email addresses: rogerson@yorku.ca (Jesse A. Rogerson), phall@yorku.ca (Patrick B. Hall)

BAL quasars themselves are distributed into three subtypes: high-ionization (HiBAL), low-ionization (LoBAL), and iron LoBAL (FeLoBAL). HiBAL quasars show absorption from only relatively high-ionization species such as C IV, N V and Si IV. LoBAL quasars also show absorption from low-ionization species such as Mg II, Al III and Al II. FeLoBAL quasars are LoBAL quasars with absorption from one or more excited states of Fe II or Fe III. Note that a range of ionization stages is seen even in HiBAL quasars, and that in LoBAL and FeLoBAL quasars the ionization simply extends to lower ionization stages (Hall et al. 2002).

Approximately 10% of quasars in optically selected samples with spectra covering rest-frame 1400-1550 Å exhibit a trough or troughs which can be considered broad absorption. The true fraction is expected to be higher due to selection effects which bias surveys against the detection of BAL quasars. Hewett and Foltz (2003) reported a corrected traditional BAL quasar fraction of $22 \pm 4\%$ using their sample of 42 bright ($B_J < 19$) BAL quasars. Reichard et al. (2003) estimated a corrected traditional BAL quasar fraction of $15.9 \pm 1.4\%$ using a sample of 224 BAL quasars with $i \lesssim 20$. Trump et al. (2006) report an uncorrected traditional BAL quasar fraction of $10.4 \pm 0.2\%$ using a sample of 1756 BAL quasars with $i \lesssim 20$, or an uncorrected fraction of $26.0 \pm 0.3\%$ using a less conservative “absorption index” criterion to define a BAL quasar (uncertainties from Poisson statistics only). By comparing the Trump et al. (2006) catalog to the near-infrared 2MASS database, Dai et al. (2008) report a corrected BAL fraction of $43 \pm 2\%$ for luminous quasars ($M_K \lesssim -30.1$) using the absorption index criterion. However, Knigge et al. (2008) find that the absorption index BAL quasar criterion includes a large number of false positives. Taking that into account, they find uncorrected and corrected BAL fractions of 13.6% and $17 \pm 3\%$. Scaling the results of Dai et al. (2008) to account for the contamination found by Knigge et al. (2008) yields a BAL fraction of 23%, which is also the upper limit BAL fraction quoted by Knigge et al. (2008). Lastly, Ganguly et al. (2007) find an uncorrected BAL fraction of 11%, corrected to 23% in Ganguly and Brotherton (2008). In summary, there is general agreement that $\approx 23\%$ of quasars exhibit BAL troughs after selection effects are taken into account.

The fraction of quasars exhibiting BAL troughs could be due to an orientation effect, such that all or most quasars have BAL outflows covering some of the lines of sight along which they would be seen as quasars (e.g., Turnshek 1986). Alternatively, it could be due to an evolutionary effect, such that all or most quasars have BAL outflows for some fraction of their lifetime (e.g., Surdej and Hutsemekers 1987). Of course, some combination of the above is also possible (e.g., Morris 1988). In any case, these outflows may have mass loss rates comparable to the accretion rates required to power quasars (Steenbrugge et al. 2005). Thus, understanding BAL quasars and BAL outflows is important for understanding quasars as a whole.

Observations show that BAL quasars are X-ray weak compared with regular quasars (e.g. Green et al. 1995, Gallagher et al. 2006, and references therein). The disk wind model of Murray et al. (1995) explains this and other properties of BAL quasars well. In that model, the X-ray weakness is attributed to intrinsic absorption from ‘hitch-hiking’ gas between the BAL outflow and the X-ray emitting region. The nearly completely ionized metal atoms in the hitch-hiking gas are kept ionized by capturing electrons and then immediately absorbing X-rays from the quasar, just as an H II region is kept ionized by protons capturing electrons and then immediately absorbing photons of energies 13.6 eV or greater. Because highly ionized metal atoms can only efficiently absorb X-rays, the hitch-hiking gas protects the BAL outflow from over-ionization by X-rays while transmitting the ultraviolet (UV) radiation that accelerates the BAL outflow to high velocities.¹ We assume a BAL quasar has an intrinsically normal X-ray spectrum but is shielded by some absorbing gas, so that constraints can be placed on the hydrogen column density required to absorb the X-ray flux.

It is also possible that some or all BAL quasars are intrinsically X-ray weak. It has been shown by

¹The hitch-hiking gas may also act as an X-ray reflector and a soft X-ray emitter, but we do not consider those effects herein.

Giustini et al. (2008) that some BAL quasars may be less X-ray absorbed than previously thought, and the X-ray weakness is due to a differing spectrum from typical quasars. The authors admit there may be some factors that could affect this result. These include the X-ray energy range used for spectral analysis, partial covering of the source by the X-ray absorber, or an ionized X-ray absorber. Streblyanska et al. (2010) go on to show that when an ionized absorber is considered, the column density of intrinsic absorption significantly increases. Although the possibility of intrinsic X-ray weakness cannot be fully rejected by current data sets, traditional BAL quasars (with $BI > 0$, where BI is the BALnicity index) appear to be always X-ray absorbed (Streblyanska et al. 2010). Both the above studies use some BAL quasars from Trump et al. (2006), which may not be actual BAL quasars (Knigge et al. 2008).

Recent sky surveys have also uncovered a slew of BAL quasars which exhibit unusual properties as compared to typical BAL quasars (e.g., Hall et al. 2002; Brunner et al. 2003; Duc et al. 2002). Investigation of these properties is as worthwhile as the study of BAL quasars themselves, as the most unusual objects will define the parameter space spanned by BAL outflows in general. If we are to have a complete understanding of quasars, our models must explain all normal and unusual quasar behaviour.

In this paper we discuss continued research into two such unusual BAL quasars. SDSS J030000.56+004828.0 (hereafter SDSS J0300+0048, Fig. 1a) is an “overlapping-trough” BAL quasar at $z = 0.89191$ with nearly complete UV absorption below rest-frame 2800 Å (Hall et al. 2002; Hall et al. 2003). This FeLoBAL quasar has a non-BAL binary companion, SDSS J025959.68+004813.6 (hereafter SDSS J0259+0048), which is located 19'5 away from SDSS J0300+0048 at a redshift $z = 0.894$ ($\Delta v = 330 \pm 160 \text{ km s}^{-1}$).

The second object is SDSS J221511.94–004549.9 (hereafter SDSS J2215–0045, Fig. 1b), a reddened FeLoBAL with detached Mg II, Al III, Al II, and Fe III UV34,48 absorption (Hall et al. 2002). This quasar is at $z = 1.4755$ as calculated by the associated Mg II absorption. SDSS J2215–0045 has absorption from Fe III but there are no absorption features from Fe II, making it a very rare and unusual find. Hall and Hutsemékers (2003) discuss how the work of de Kool et al. (2002) shows that the presence of Fe III but lack of Fe II absorption restricts the outflow to high densities and a narrow range of column densities.

X-ray data has been obtained using the Chandra X-ray Observatory and analyzed to help understand these two unusual BAL quasars. We discuss our data and methods in §2, present the results of our observations in §3 and §4, discuss their implications in §5 and summarize our results in §6. We adopt the cosmology of Spergel et al. (2007): $H_0 = 73.2$, $\Omega_M = 0.259$, and $\Omega_\Lambda = 0.741$.

2. X-ray Data and Analysis

Observations of our two targets were carried out in Chandra Cycle 4 using the Advanced CCD Imaging Spectrometer (ACIS).

We use the observed-frame energy range 0.5–6.65 keV: 0.5 keV is an obvious lower energy cutoff due to the increased background (and higher throughput degradation) at low energies, and 6.65 keV was chosen as the upper limit because it has the same effective area as the 0.5 keV lower limit and because the effective observing area drops quickly at energies > 6.65 keV. The source count rate in the energy range 0.5–6.65 keV is expected to be a factor of 100 higher than in the range 6.65–13 keV, while the expected background count rate is the same in these energy ranges.²

Given the small number of detections of X-ray photons over a finite time period, we are limited by small-number statistics rather than by the background level. To determine upper limits at specified confidence intervals in the face of small-number statistics, we use the Bayesian method of Kraft et al. (1991) rather than

²See <http://cxc.harvard.edu/proposer/POG/html/index.html>

the frequentist method outlined in Gehrels (1986). The Bayesian method is favored due to its ability to work with non-zero background flux when in the zero source count regime.

2.1. AGN X-ray-UV Luminosity Correlation

The X-ray and UV luminosities of regular (non-BAL) quasars are observed to have a strong correlation across multiple decades of UV luminosity; this offers a useful tool for measuring the X-ray weakness of a BAL quasar, which tend to have far weaker X-ray luminosity than a typical quasar. The correlation is usually expressed in terms of the logarithm of the ratio between the 2 keV ($l_{2\text{keV}}$) and 2500Å (l_{2500}) rest-frame specific luminosities, denoted as α_{ox} :

$$\alpha_{ox} = 0.372 \log(l_{2\text{keV}}/l_{2500}) \quad (1)$$

This correlation has been quantified carefully in a recent study by Steffen et al. (2006) by observing the $l_{2\text{keV}}$ and l_{2500} of 333 AGNs (from multiple surveys). The best fit to the data is:

$$\log(l_{2\text{keV}}) = (0.721 \pm 0.011) \log(l_{2500}) + (4.531 \pm 0.688) \quad (2)$$

Thus, provided a UV luminosity, the expected X-ray luminosity can be calculated. For typical quasars, α_{ox} can be written as a function of l_{2500} , as in Steffen et al. (2006):

$$\alpha_{ox}(UV) = (-0.137 \pm 0.008) \log(l_{2500}) + (2.638 \pm 0.240) \quad (3)$$

To characterize the X-ray weakness we compare the observed α_{ox} value, calculated using the observed l_{2500} and $l_{2\text{keV}}$ in equation (1), to the expected α_{ox} value $\alpha_{ox}(UV)$. The difference between the two is denoted $\Delta\alpha_{ox}$:

$$\Delta\alpha_{ox} = \alpha_{ox} - \alpha_{ox}(UV) \quad (4)$$

By exploiting the strong correlation between l_{2500} and $l_{2\text{keV}}$ in ordinary quasars, we can quantify the X-ray weakness of our targets.

To determine l_{2500} for our targets requires estimating f_{2500} for their underlying continua. We used the spectra available for each object in SDSS Data Release Six (Adelman-McCarthy et al. 2008). We used either the smoothed or extrapolated flux at 2500 Å rest-frame as f_{2500} ; details are given in the individual objects' discussions below. We have assumed a value of 10% as the uncertainty on the UV flux for the following discussion. The luminosity distance to each quasar was calculated following Pen (1999) based on the quasar's redshift and our adopted cosmology.

3. Results: SDSS J0300+0048 and SDSS J0259+0048

SDSS J0300+0048 and SDSS J0259+0048 were observed simultaneously for 6743.5 seconds on December 19, 2002 (UT). No X-ray photons were detected within a 2'5 radius of the position of SDSS J0300+0048. SDSS J0259+0048 was detected, with 39 photons within 2'5 of its position. The measured background of the image is such that we expect only 0.244 ± 0.014 observed-frame 0.5-6.65 keV background photons in the detection apertures.

3.1. Results: SDSS J0259+0048

We first analyze the SDSS J0259+0048 results, as it is a non-BAL quasar and is thus expected to be unremarkable. As a test of our methods, we seek to reproduce the observed X-ray photon count of 39, by using only the observed UV flux and the relations in §2.1.

For this quasar at $z = 0.894$ we find $f_{2500} = (0.55 \pm 0.05) \times 10^{-27} \text{ erg s}^{-1} \text{ cm}^{-2} \text{ Hz}^{-1}$ and $l_{2500} = (2.00 \pm 0.20) \times 10^{30} \text{ erg s}^{-1} \text{ Hz}^{-1}$.

Using equation (2) we therefore expect $\log(f_{2\text{keV}}) = -31.2^{+0.8}_{-0.7} \text{ erg s}^{-1} \text{ cm}^{-2} \text{ Hz}^{-1}$. Given the predicted X-ray flux, we expect 2.8 times the observed count rate of 1.59 in the log, but the difference is $< 1\sigma$. Thus, our method accurately reproduces the observed X-ray photon count of an unremarkable quasar.

Using equation (1) we calculated an observed $\alpha_{ox} = -1.63 \pm 0.04$ for SDSS J0259+0048. The expected α_{ox} is calculated by equation (3). Plugging in the observed l_{2500} we expect $\alpha_{ox}(UV) = -1.51 \pm 0.34$. Thus $\Delta\alpha_{ox} = -0.12 \pm 0.34$. Therefore, within the uncertainties, the observed and expected values for α_{ox} (and X-ray counts) are the same.

3.2. Results: SDSS J0300+0048

Using the same method as above, we analyze the observed and predicted X-ray quantities for the FeLoBAL quasar SDSS J0300+0048 at $z = 0.89194$ to determine the column density of the intervening matter.

The ‘‘detection’’ of zero photons in the image results in an upper limit of 3.00 photons at 95% confidence (Kraft et al. 1991), equivalent to a count rate of $\leq 4.445 \times 10^{-4} \text{ photons s}^{-1}$ in the observed bandpass. This corresponds to an observed X-ray flux upper limit of $f_{2\text{keV}} \leq 1.793 \times 10^{-33} \text{ erg s}^{-1} \text{ cm}^{-2} \text{ Hz}^{-1}$ at 95% confidence.

To find f_{2500} we fit a power law in f_ν to narrow normalization windows centered at 3060 Å and 4735 Å rest-frame. The resulting flux at 2500 Å is $f_{2500} = (3.77 \pm 0.38) \times 10^{-27} \text{ erg s}^{-1} \text{ cm}^{-2} \text{ Hz}^{-1}$.

Equation (2) then predicts the X-ray flux of SDSS J0300+0048 to be $\log(f_{2\text{keV}}) = -30.58^{+0.77}_{-0.79} \text{ ergs s}^{-1} \text{ cm}^{-2} \text{ Hz}^{-1}$, which includes the uncertainty in the power law slope in the UV band. Therefore, we expect to see $2.6^{+0.8}_{-0.7}$ X-ray counts in the log in the image. This is higher than the observed 95% confidence limit of 0.5 in the log.

We characterize this X-ray weakness as follows. The expected α_{ox} (from equation 3) is $\alpha_{ox}(UV) = -1.64 \pm 0.35$ and the observed α_{ox} (from equation 1) is $\alpha_{ox} \leq -2.35$ at 95% confidence. Therefore the deviation of the observed α_{ox} from the predicted value is $\Delta\alpha_{ox} \leq -0.72$, which is a reduction in $f_{2\text{keV}}$ by a factor of 164 from the expected flux. This reduction in X-ray flux is attributed to shielding gas near the quasar, which must have a hydrogen column density of $N_H \geq 1.8 \times 10^{24} \text{ cm}^{-2}$ at the quasar redshift, assuming solar metallicity. That lower limit was calculated assuming neutral gas, but applies to neutral or ionized gas. If the gas is partly or fully ionized, it will absorb fewer photons per unit column density, and therefore the required minimum column density will be larger than the above lower limit.

Gibson et al. (2009) report $\alpha_{ox} \leq -2.33$ and $\Delta\alpha_{ox} \leq -0.70$ for this object in their summary of BAL quasars from SDSS data release 5. The values are slightly different from values quoted in this paper because slightly different formulae were used. Nevertheless, the values are consistent within the uncertainties.

We can compare our result with the column densities required to explain the UV absorption, in particular the Ca II column density $N_{CaII} = (7.13 \pm 1.15) \times 10^{14} \text{ cm}^{-2}$ (Hall et al. 2003). Because its ionization potential is less than that of H I, Ca II becomes the dominant calcium ion only at large columns behind an H I ionization

³<http://cxc.harvard.edu/toolkit/pimms.jsp>: the online version of Portable, Interactive Multi-Mission Simulator, providing count-rate estimations and predictions for *Chandra*.

front (§5.2 of Hall et al. 2003). Ferland and Persson (1989) found that for clouds of density $10^{9.5} \text{ cm}^{-3}$, Ca II is dominant only at a column densities $N_H \geq 6.3 \times 10^{24} \text{ cm}^{-2}$, more than a factor of ten higher than the column density of the H I ionization front.

We have used the photoionization simulator CLOUDY⁴ to investigate the absorption in various ions for a representative Broad Line Region (BLR) (density of $n_e = 10^{11} \text{ cm}^{-3}$, $\log U = -1.5$, where U is the ionization parameter) (Baldwin et al. 2003). Note that our CLOUDY simulations were run with solar metallicity and no dust obscuration. Even at $N_H = 10^{25} \text{ cm}^{-2}$, Ca II is not the dominant calcium ion. However, the ionic fraction of Ca II immediately behind the H I ionization front is $\sim 1\%$ for $n_e = 10^{11} \text{ cm}^{-3}$, significantly higher than the $\sim 0.3\%$ seen for $n_e = 10^{9.5} \text{ cm}^{-3}$. Given that the abundance of Ca II is -5.64 in the log, each $N_H = 10^{22} \text{ cm}^{-2}$ behind the H I ionization front yields $10^{(22-2-5.64)}$ worth of Ca II: $N_{CaII} = 2.29 \times 10^{14} \text{ cm}^{-2}$. Ca I has a similar behavior to Ca II though its ionic abundance immediately behind the H I ionization front is only 0.0001%.

Thus, to match the Ca II column observed in SDSS J0300+0048 with standard BLR parameters requires only $N_H = 3.11 \times 10^{22} \text{ cm}^{-2}$ behind the hydrogen ionization front. This agrees with the constraint on the total N_H behind the front from the observed upper limit on the Ca I column density: $N_H \leq 7 \times 10^{23} \text{ cm}^{-2}$.

However, the UV-derived $N_H \simeq 3.11 \times 10^{22} \text{ cm}^{-2}$ is much less than the X-ray-derived $N_H \geq 1.8 \times 10^{24} \text{ cm}^{-2}$. This can be explained by assuming a higher ionization parameter at the cloud face. Using CLOUDY, we investigated the behavior of Ca II with higher values for the ionization parameter; namely $\log U = 0.5, 1.0, 1.5$, and 2.0 . We also varied the density: separate runs for a density of $n_e = 10^{11} \text{ cm}^{-3}$ and $n_e = 10^{12} \text{ cm}^{-3}$ were carried out for each of the above values of $\log U$. The results are shown in Figure 2.

The shaded regions are defined by the UV-derived Ca II column density (horizontal region) and the X-ray derived lower limit on the hydrogen column density (vertical regions). The lower limit on the hydrogen column is shown at 1σ (lightest grey), 2σ , and 3σ (darkest grey). The curves represent the different $\log U$ of interest for this object. For a specific $\log U$ to match the observations, its curve must fall in the allowed region for both the column densities plotted. In Figure 2, the allowed region for each $\log U$ is represented by a cyan highlight. Thus, this object requires $\log U > 0.0$ for both $n_e = 10^{11} \text{ cm}^{-3}$ and $n_e = 10^{12} \text{ cm}^{-3}$ (Figures 2a and 2b, respectively). This lower limit is consistent with the constraints posed by Ca I (plotted in Figure 3), and also the constraints from absorption in Mg I, Mg II, and Fe II.

However, as we shall see in § 5.1, observations of Fe II* rule out the $\log U > 0$, $n_e \simeq 10^{11} \text{ cm}^{-3}$ scenario; gas with such parameters may form part of the absorber in this object, but it cannot form the entire absorber.

4. Results: SDSS J2215–0045

SDSS J2215–0045 was observed for 6615.9 seconds on June 21, 2003 (UT). The measured background of the image is such that we expect only 0.102 ± 0.004 observed-frame 0.5–6.65 keV background photons in the detection apertures.

To find f_{2500} we fit a power law in f_ν to narrow normalization windows centered at 2668 Å and 3035 Å rest-frame. The result is $f_{2500} = (7.26 \pm 0.73) \times 10^{-27} \text{ erg s}^{-1} \text{ cm}^{-2} \text{ Hz}^{-1}$. The true f_{2500} could be somewhat higher since we do not account for possible Mg II absorption in the shorter-wavelength normalization region, nor do we account for the inferred continuum reddening of $E(B-V) \simeq 0.06$ (Hall and Hutsemékers 2003). Accounting for either of those effects would increase f_{2500} , which would increase the predicted $f_{2 \text{ keV}}$, which would in turn increase the absorption needed to bring the predicted $f_{2 \text{ keV}}$ below the upper limit we measure. Thus, this value of f_{2500} is conservative with respect to the amount of X-ray absorption we infer.

⁴<http://www.ferland.org/cloudy/>

No photons are detected in the observed 0.5–6.65 keV bandpass, so we have a conservative upper limit of 3.00 photons at 95% confidence.⁵ This limit corresponds to a count rate of $\leq 4.544 \times 10^{-4}$ photons s^{-1} . The observed X-ray flux limit is therefore $f_{2\text{keV}} \leq 1.776 \times 10^{-33}$ erg s^{-1} cm^{-2} Hz^{-1} . From the observed X-ray flux upper limit we calculate the observed α_{ox} upper limit, using equation (1), and find $\alpha_{ox} \leq -2.45$ at 95% confidence.

The expected X-ray flux is $\log(f_{2\text{keV}}) = -30.53^{+0.78}_{-0.77}$ erg s^{-1} cm^{-2} Hz^{-1} , which includes the uncertainty in the power law slope in the UV band. Given that flux, $2.70^{+0.77}_{-0.80}$ counts in the log should be observed over 6615.9s, which is higher than the observed 95% confidence limit of 0.5 in the log. We also expect $\alpha_{ox}(UV) = -1.74 \pm 0.35$. The deviation of the observed α_{ox} from the predicted value is $\Delta\alpha_{ox} \leq -0.71$. Compared to SDSS J0300+0048, we probe higher-energy photons in SDSS J2215–0045 due to its higher redshift, and so to produce the same observed $\Delta\alpha_{ox} \leq -0.71$ requires a higher absorbing column: $N_H \geq 3.4 \times 10^{24}$ cm^{-2} at the quasar redshift, assuming solar metallicity. Again, this is a hard lower limit assuming a neutral absorber.

Gibson et al. (2009) also evaluated values for this object. They find $\alpha_{ox} < -2.71$ and $\Delta\alpha_{ox} \leq -0.96$. Again, due to slightly different formulae, the values derived in Gibson et al. (2009) are slightly different than those calculated here. In this case, the $\Delta\alpha_{ox}$ value is $< 1.5\sigma$ different.

The presence of doubly ionized iron (Fe III) absorption without any significant singly ionized iron (Fe II) absorption is a rare occurrence. de Kool et al. (2002) showed that this iron absorption behaviour could be produced with a density of $n_e = 10^{11}$ cm^{-3} , an ionization parameter $\log U = -1.5$, and a very narrow range of total hydrogen column density around $\log N_H \sim 22.4$. We investigated this result with CLOUDY simulations using the same parameters as for SDSS J0300+0048. The results for Fe III are located in Figure 4 and the results for Fe II in Figure 5.

In Figure 4, the shaded region is shaped by the lower limits of both the X-ray derived hydrogen column (vertical lower limits) and the UV-derived Fe III column density (horizontal lower limits; details given in § 5.2). The curves must fall inside this region to correctly describe the observations. The curves must also satisfy the upper limit on the Fe II column density (also discussed in § 5.2) shown in Figure 5. The shaded region, in this case, is defined by an upper limit Fe II column.

The cyan segments in Figure 4 represent the interval over which each curves match the observations by falling within the shaded regions of both Figures 4 and 5. We can place a lower limit of $\log U > 1.0$ on the ionization parameter for both the $n_e = 10^{11}$ cm^{-3} and $n_e = 10^{12}$ cm^{-3} cases (Figures 5a and 5b, respectively). This lower limit is consistent with constraints imposed by Mg II, Al II, and Al III.

The physical basis behind these constraints is that Fe III absorption without significant Fe II absorption is seen when the absorber has just barely enough column density to form a hydrogen ionization front, because Fe III is only abundant just before such a front and Fe II is abundant just after one. Furthermore, to create an Fe III column matching the observations in the narrow region just before the front requires a high density, because such high densities force Fe IV to recombine to Fe III (Bautista and Pradhan 1998).

5. Discussion

We have shown that both SDSS J0300+0048 and SDSS J2215–0045 are undetected in snapshot X-ray observations. Despite the short exposure times of the X-ray observations, non-detections of these optically bright quasars require very large absorbing columns and small levels of unabsorbed X-ray scattering ($< 1.3\%$ at 95% confidence).⁶ Note that our column density lower limits assume neutral absorption. As shown by

⁵One photon with energy 12.7 keV is detected within 2'' of the position of SDSS J2215–0045, but photons with such high energies are much more likely to be background photons, as discussed in §2.

Streblyanska et al. (2010), when an ionized absorber model is used, BAL quasar X-ray absorbing columns can be 1-2 orders of magnitude larger than in the neutral case. Thus, the column densities we quote here are hard lower limits, and the true column densities are almost certainly larger. We now discuss the implications of these results in more detail.

5.1. SDSS J0300+0048

In SDSS J0300+0048, at outflow velocities of $2000 < v < 4000 \text{ km s}^{-1}$ we see Mg II, Mg I, Ca II and Fe II absorption. At $4000 < v \lesssim 10850 \text{ km s}^{-1}$, we see Mg II, Fe II and excited-state Fe II (Fe II*) absorption from gas which must be located closer to the quasar than the Ca II-absorbing region. (If it were located farther from the quasar than the Ca II-absorbing region, it would be shielded by that gas and would itself show Ca II.)

Hall et al. (2003) and Hall and Hutsemékers (2004) suggested that the SDSS J0300+0048 outflow could be produced by gas in an accretion disk wind if we are looking across the wind rather than down the wind. In this model, high-ionization gas is launched from closer to the quasar than low-ionization gas is, with Ca II and Mg I being launched from outside a hydrogen ionization front.⁷

We can constrain the density in the Fe II*-absorbing region by studying the critical densities of excited levels from which we either see or do not see Fe II* absorption. We see absorption from the Fe II UV78 multiplet, whose lower level has a critical density of $\approx 10^{5.5} \text{ cm}^{-3}$. We do not see absorption from Fe II UV195/UV196 multiplets, with relevant critical densities of $\approx 10^{7.5} \text{ cm}^{-3}$. Thus, we can constrain the density in the Fe II*-absorbing region to be $\approx 10^{6.0 \pm 0.5} \text{ cm}^{-3}$.

We now examine the ionization behaviour of a slab of gas at this density, to see if a single-slab model can explain both the X-ray and UV absorption. In Figure 6 we present two CLOUDY runs for $n_e = 10^6 \text{ cm}^{-3}$, with $\log U = 1.0$ and $\log U = -0.5$. For $\log U = 1.0$, the observed Fe II column (Figure 6a) can be reached with reasonable hydrogen column densities, but the Ca II column (Figure 6b) can only be achieved with $N_H \sim 10^{25} \text{ cm}^{-2}$. When the hydrogen column approaches $\sim 10^{25} \text{ cm}^{-2}$ between us and the quasar UV emission region, the electron scattering optical depth rises above $\tau_{es} \sim 2$, increasing the already high intrinsic optical and UV luminosity of this object. (Of course, the X-ray absorption may cover only the X-ray continuum-emitting region, and not the larger UV continuum-emitting region, but at the moment we are only considering whether a single uniform absorber can explain the data.) For $\log U = -0.5$, the observed Ca II column (Figure 6b) is reached at $\sim 3 \times 10^{24} \text{ cm}^{-2}$, at which point the predicted Fe II column is well above the observationally inferred lower limit and the temperature within a factor of two of the observationally inferred upper limit.

Thus, in light of the X-ray data, we find that we can nearly match the properties of both the X-ray and UV absorbers in SDSS J0300+0048 with one slab of gas of constant density $n_e = 10^6 \text{ cm}^{-3}$ with $\log U = -0.5$ at its ionized face, implying an absorber at a distance of $\sim 60 \text{ pc}$ from the black hole with a thickness of $\sim 3 \times 10^{18} \text{ cm}$ or $\sim 1 \text{ pc}$.

If the absorbing gas in SDSS J0300+0048 can be approximated by gas with a uniform density of $n_e = 10^6 \text{ cm}^{-3}$, it is difficult to reconcile the resulting $\sim 60 \text{ pc}$ distance of the gas from the black hole with the

⁶These X-ray scattering constraints are broadly consistent with optical polarization measurements for both objects (Hall, Smith, et al., unpublished): SDSS J0300+0048 has R -band $P = 1.58 \pm 0.10\%$ and SDSS J2215–0045 has a white-light $P = 0.40 \pm 0.06\%$.

⁷The radial dependence of the density in the outflow at launch is unclear. As mentioned in Hall et al. (2003), in region (a) of a Shakura and Sunyaev (1973) disk the density increases with radius. A disk wind launched from that region would have a higher density in the Ca II region than in the Fe II* region. A low temperature ($T \lesssim 1100 \text{ K}$) would be required in the Ca II region to avoid exciting Fe II* there. On the other hand, the low-ionization absorption in this object covers the Mg II (and Fe II) broad emission line region, located at radii where the Shakura and Sunyaev (1973) disk model predicts a radially decreasing density. If the disk wind is launched at these larger radii and its density is decreasing with distance, the density in the Ca II-absorbing region should be the lowest in the outflow. A density of $n_e \lesssim 10^3 \text{ cm}^{-3}$ would be required to avoid populating the lower levels of Fe II* transitions which are not observed.

original disk wind scenario of Hall et al. (2003). Such a distance is more consistent with the alternative scenario to a disk wind discussed in Hall et al. (2003); namely, that the outflow sweeps up gas at large distances from its origin and decelerates in the process. In this swept-up-gas scenario, the Fe II*-absorbing gas would be gas which has been compressed to $n_e \gtrsim 10^3 \text{ cm}^{-3}$ and accelerated to $4000 < v < 10850 \text{ km s}^{-1}$ by a high-ionization, low-density wind (seen at velocities up to at least $v = 10850 \text{ km s}^{-1}$ in this object). The Ca II-absorbing gas would be gas which has been overtaken by the wind more recently and which has therefore been compressed and accelerated to a lesser degree than the Fe II*-absorbing gas. However, it remains to be seen (through detailed outflow modeling beyond the scope of this investigation) whether gas can be accelerated to $2000 < v < 4000 \text{ km s}^{-1}$ without being compressed to a density $n_e > 10^3 \text{ cm}^{-3}$ or heated to a temperature $T > 1100 \text{ K}$. Meanwhile, as suggested by Hall et al. (2003), this swept-up-gas scenario can be tested by looking for a long-term increase of the Ca II BAL outflow velocity. (No increase was seen over a rest-frame time span of up to 205 days in multiple SDSS spectra plus our VLT spectrum of this object.)

5.2. SDSS J2215–0045

The conservative upper limit of $\log N_{\text{FeII}} < 14.7$ (Figure 5) for this object was estimated using the plausible unabsorbed continuum from Hall and Hutsemékers 2003 (hereafter HH03), shown in Figure 1b. The details of the estimation of the lower limits for the Fe III column density shown in Figure 4 are given in the Appendix.

We have found in §4 that if a single absorber is responsible for both the observed UV and X-ray absorption in SDSS J2215–0045, it must have $N_H > 3.4 \times 10^{24} \text{ cm}^{-2}$, $\log n_e \gtrsim 9.5 \text{ cm}^{-3}$ and $\log U \gtrsim 1$, with full coverage of the X-ray source and at least 50% coverage of the UV continuum source. We now consider whether an absorption system with those properties is in fact plausible.

If we take $N_H = 3 \times 10^{24} \text{ cm}^{-2}$ and $\log n_e = 9.5 \text{ cm}^{-3}$, then the absorber is only 10^{15} cm thick. A larger N_H would make for a thicker absorber but would also increase the electron scattering optical depth above $\tau_{es} \simeq 2$, increasing the already high intrinsic luminosity of this quasar. The X-ray continuum region is $\sim 10^{15} \text{ cm}$ in radius (Chartas et al. 2009), while the UV continuum region is $\sim 10^{16} \text{ cm}$ in radius (Kochanek et al. 2007). To cover both regions, the absorber would have to be at least 20 times larger in the transverse direction than it is in the line-of-sight direction. Moreover, the line-of-sight velocity width of the absorber is $12,000 \text{ km s}^{-1}$. If that is a turbulent Δv , the absorber would double its thickness and halve its density on a timescale equal to the crossing time of ~ 10 days, but observations of SDSS J2215–0045 over rest-frame timescales much longer than that reveal no changes in its absorption troughs (HH03). If that Δv is a coherent velocity spread along our line of sight, the acceleration required to produce it in 10^{15} cm is $\sim 100 \text{ m s}^{-2}$. For comparison, in the disk wind model of Murray et al. (1995) the radiative acceleration is $\lesssim 100 \text{ cm s}^{-2}$.

It is hard to see how to bring the above extreme parameters into the realm of the plausible. For example, a supersolar Fe abundance would reduce the N_H required to match the observed N_{FeIII} , and Ly α pumping of Fe III UV34 (Johansson et al. 2000) would reduce the amount of Fe needed to explain a given N_{FeIII} . Those effects could eliminate the τ_{es} problem, but would shrink the line-of-sight width of the absorber and make the dynamical problems worse.

Thus, a single, uniform absorber with the properties required to explain the UV and X-ray absorption in this system is extremely unlikely to exist. Instead, it is likely that the X-ray absorber is Compton-thick ($\gtrsim 3 \times 10^{24} \text{ cm}^{-2}$) but compact (radius $\sim 10^{15} \text{ cm}$), so that at most a small part of the UV continuum region is obscured by it. The UV absorber must be larger (radius $\sim 10^{16} \text{ cm}$) and have a column density just under that required to form a hydrogen ionization front ($N_H \lesssim U \times 10^{23} \text{ cm}^{-2}$) so that it contains very little Fe II. We can constrain $-1 \lesssim \log U \lesssim 1$ for the UV absorber. The upper limit comes from setting the electron scattering optical depth to the UV continuum source to be at most unity. The lower limit comes via our

measured $\log N_{\text{FeIII}} > 16.62$ and $\log N_{\text{FeII}} < 14.7$; given those values, Table 2 of de Kool et al. (2002) and our Figures 5 and 4 show that $\log n_e \gtrsim 9.5 \text{ cm}^{-3}$ and $\log U \gtrsim -1$.⁸

We can reconcile the high density required for the Fe III column with the large velocity and velocity spread of Fe III if we assume the Fe III absorption arises in dense clumps embedded in a lower density, higher ionization wind seen in C IV and Si IV, along the lines suggested by Voit et al. (1993). The clump widths along the line of sight would be $d < N_H/n_e$, or $d < 10^{13.5 \pm 1.0} \text{ cm}$. This maximum size is larger than the typical size of 10^{12} cm predicted for putative BLR clouds (Korista et al. 1997). To cover half the $r \sim 10^{16} \text{ cm}$ UV source, a large number of such clumps ($\sim 10^{5 \pm 2}$ if the clumps are roughly spherical) are required.

In this object, Fe III absorption is seen at $6000 < v_{\text{FeIII}} < 18000 \text{ km s}^{-1}$ along our line of sight, whereas C IV and Si IV absorption is seen at $0 < v < 25000 \pm 3000 \text{ km s}^{-1}$ (Figure 1 of HH03). Given that the troughs in this object have higher outflow velocities and velocity widths than the average BAL trough, it is reasonable to assume that much of the acceleration of the gas occurs along our line of sight; in other words, the outflow streamlines are largely parallel to our line of sight. If we imagine an accelerating, relatively low density wind (seen in C IV and Si IV) colliding with dense Fe III clumps, the wind will form a shock around the clumps and can in principle accelerate, ablate, compress and bypass the clumps. The acceleration may help explain the Fe III trough velocity, along with radiative and possibly magnetohydrodynamic acceleration; the ablation helps explain the Fe III trough width; the compression helps explain the inferred high densities; and the bypassing explains the C IV and Si IV trough extending to both smaller and larger outflow velocities than the Fe III trough (Voit et al. 1993).

In summary, our picture of this quasar is that the X-ray-emitting region is completely covered by an X-ray absorber and that the more distant UV-emitting region is nearly or completely covered by a UV-absorbing wind seen in C IV and Si IV absorption. This wind is accelerated (at least in part along our line of sight) from 0 km s^{-1} to $25000 \pm 3000 \text{ km s}^{-1}$. At some distance or range of distances from the quasar, the wind includes dense, Fe III-emitting clumps (with overall covering factor $\sim 50\%$ and low volume filling factor) which have been accelerated by the wind to velocities of $6000 < v_{\text{FeIII}} < 18000 \text{ km s}^{-1}$. A paraboloidal shock surrounds each clump, where the wind gas encounters the slower-moving clump gas. The shock-heated gas is no longer visible in C IV or Si IV, but between a clump and its shock lies a region where gas ablated from the clump will absorb in those ions, at velocities $v \simeq v_{\text{FeIII}}$. The wind downstream from the clumps — consisting of shocked gas and, if the volume filling factor of the clumps is small, unshocked gas as well — is not seen to recombine to observable ionization stages when shadowed by a clump, so its recombination timescale must be longer than the time it spends in a shadow.

In this picture, the Fe III-emitting clumps are being ablated and so the Fe III trough depth will decrease with time unless the wind encounters new clumps. Such clumps should first appear at low velocity; from their absence, we conclude that the wind is not currently encountering new clumps. Spectroscopic monitoring of the quasar to look for weakening Fe III troughs (as well as any changes in Fe III trough velocity or velocity width) would be worthwhile.

Lastly, we note the possibility that this quasar may have developed from a typical FeLoBAL. In such an object, Fe II is seen at low velocities and C IV at both high and low velocities, consistent with a high-ionization wind which has encountered clouds optically thick in the Lyman limit and has only begun to accelerate them. As time progresses, the clouds will be accelerated and ablated. Eventually, they may be optically thin in the Lyman limit (and thus seen in Fe III and not Fe II) and will be found at higher velocities.

⁸We assume that the UV absorber is fully shielded by a dust-free X-ray absorber. In that case, the X-ray absorber will absorb a relatively small fraction of hydrogen-ionizing photons, and the structure of the absorber's Stromgren sphere will be much less affected than the structure of its partially ionized zone. We can therefore use our constant-density CLOUDY simulations to infer the conditions of the Fe III clumps, even though the higher-ionization regions in the outflow must have a lower density.

6. Conclusion

SDSS J0300+0048 and SDSS J2215–0045 have some of the highest known column densities in their BAL outflows.

SDSS J0300+0048 specifically has a very high Mg II absorbing column, which creates the overlapping absorption below rest-frame 2800Å. Exploiting the correlation between X-ray and UV luminosities, we find $\Delta\alpha_{ox} < -0.72$, indicating strong X-ray absorption. The X-ray absorbing gas must have a column density of $N_H \geq 1.8 \times 10^{24} \text{ cm}^{-2}$ (assuming solar metallicity). Absorption from Fe II UV78 but not Fe II UV195/UV196 in the UV spectra indicates a density in this absorbing region of $n_e \simeq 10^6 \text{ cm}^{-3}$. We have provided two CLOUDY runs at this density with ionization parameters $\log U = 1.0$ and $\log U = -0.5$. Most properties of the absorber in SDSS J0300+0048 can be matched with a slab of gas of constant density $n_e = 10^6 \text{ cm}^{-3}$ with $\log U = -0.5$ at its ionized face (implying a distance of ~ 60 pc from the black hole) and a thickness of $3 \sim 10^{18} \text{ cm}$ (~ 1 pc).

For SDSS J2215–0045, we showed that a single absorbing slab of density $\log n_e \geq 9.5 \text{ cm}^{-3}$ and $\log U \geq 1$ that fully covers the X-ray source and covers at least 50% of the UV continuum could explain the total hydrogen column and Fe II+Fe III column densities. These parameters are shown to have little physical plausibility, as they require an abnormally high acceleration to produce the observed line-of-sight velocity spread seen in the UV absorption troughs (the velocity spread would otherwise disperse the slab and reduce its density on extremely short timescales). One possible scenario to explain the absorption would be dense Fe III-emitting clumps inside a lower density UV-absorbing wind (seen in C IV and Si IV absorption). The UV wind is accelerated from 0 km s^{-1} to $25000 \pm 3000 \text{ km s}^{-1}$, and impacts the the denser Fe III clumps. The clumps are accelerated to the observed velocity dispersion while being ablated by the UV wind. Such a model could be tested by looking for evaporation of the dense Fe III absorbing clumps manifesting itself as time-varying absorption features in the UV spectra. Explaining the rarity of Fe III-dominant BAL quasars is easier: only a small parameter space for strong Fe III absorption with little Fe II absorption present is found by both de Kool et al. (2002) and our own CLOUDY runs.

We thank M. Bautista for discussions regarding Fe III. PBH acknowledges the hospitality of the University of Wyoming Department of Physics and Astronomy and the Aspen Center for Physics, where parts of this work were completed. PBH acknowledges financial support from a Fundación Andes grant and from NSERC; PBH and MSB acknowledge financial support from Chandra (proposal 04700849). This research made use of the Atomic Line List v2.04 at <http://www.pa.uky.edu/~peter/atomic/>.

References

- Adelman-McCarthy, J., Agüeros, M., Allam, S., Allende Prieto, C., Anderson, K., Anderson, S., Annis, J., Bahcall, N., Bailer-Jones, C., Apr. 2008. The Sixth Data Release of the Sloan Digital Sky Survey. *Astrophys. J. Suppl. Ser.* 175, 297–313.
- Baldwin, J. A., Ferland, G. J., Korista, K. T., Hamann, F., Dietrich, M., Jan. 2003. The Mass of Quasar Broad Emission Line Regions. *Astrophys. J.* 582, 590–595.
- Bautista, M. A., Pradhan, A. K., Jan. 1998. Ionization Structure and Spectra of Iron in Gaseous Nebulae. *Astrophys. J.* 492, 650–676.
- Brunner, R. J., Hall, P. B., Djorgovski, S. G., Gal, R. R., Mahabal, A. A., Lopes, P. A. A., de Carvalho, R. R., Odewahn, S. C., Castro, S., Thompson, D., Chaffee, F., Darling, J., Desai, V., Jul. 2003. Peculiar Broad Absorption Line Quasars Found in The Digitized Palomar Observatory Sky Survey. *Astron. J.* 126, 53–62.
- Chartas, G., Kochanek, C. S., Dai, X., Poindexter, S., Garmire, G., Mar. 2009. X-Ray Microlensing in RXJ1131-1231 and HE1104-1805. *Astrophys. J.* 693, 174–185.
- Dai, X., Shankar, F., Sivakoff, G. R., Jan. 2008. 2MASS Reveals a Large Intrinsic Fraction of BALQSOs. *Astrophys. J.* 672, 108–114.

- de Kool, M., Becker, R. H., Arav, N., Gregg, M. D., White, R. L., May 2002. Keck HIRES Spectroscopy of the Fe II Low-Ionization Broad Absorption Line Quasar FBQS 0840+3633: Evidence for Two Outflows on Different Scales. *Astrophys. J.* 570, 514–525.
- Duc, P.-A., Hall, P. B., Fadda, D., Chaniai, P., Elbaz, D., Monaco, P., Pompei, E., Poggianti, B. M., Flores, H., Franceschini, A., Biviano, A., Moorwood, A., Cesarsky, C., Jul. 2002. An unusual iron Lo-BAL quasar detected by ISOCAM. *Astron. Astrophys.* 389, L47–L50.
- Ferland, G. J., Persson, S. E., Dec. 1989. Implications of CA II emission for physical conditions in the broad-line region of active galactic nuclei. *Astrophys. J.* 347, 656–673.
- Gallagher, S. C., Brandt, W. N., Chartas, G., Priddey, R., Garmire, G. P., Sambruna, R. M., Jun. 2006. An Exploratory Chandra Survey of a Well-defined Sample of 35 Large Bright Quasar Survey Broad Absorption Line Quasars. *Astrophys. J.* 644, 709–724.
- Ganguly, R., Brotherton, M. S., Jan. 2008. On the Fraction of Quasars with Outflows. *Astrophys. J.* 672, 102–107.
- Ganguly, R., Brotherton, M. S., Cales, S., Scoggins, B., Shang, Z., Vestergaard, M., Aug. 2007. Outflows and the Physical Properties of Quasars. *Astrophys. J.* 665, 990–1003.
- Gehrels, N., Apr. 1986. Confidence limits for small numbers of events in astrophysical data. *Astrophys. J.* 303, 336–346.
- Gibson, R. R., Jiang, L., Brandt, W. N., Hall, P. B., Shen, Y., Wu, J., Anderson, S. F., Schneider, D. P., Vanden Berk, D., Gallagher, S. C., Fan, X., York, D. G., Feb. 2009. A Catalog of Broad Absorption Line Quasars in Sloan Digital Sky Survey Data Release 5. *Astrophys. J.* 692, 758–777.
- Giustini, M., Cappi, M., Vignali, C., Nov. 2008. On the absorption of X-ray bright broad absorption line quasars. *Astron. Astrophys.* 491, 425–434.
- Green, P. J., Schartel, N., Anderson, S. F., Hewett, P. C., Foltz, C. B., Brinkmann, W., Fink, H., Truemper, J., Margon, B., Sep. 1995. The Soft X-Ray Properties of a Large Optical QSO Sample: ROSAT Observations of the Large Bright Quasar Survey. *Astrophys. J.* 450, 51.
- Hall, P. B., Anderson, S. F., Strauss, M. A., York, D. G., Richards, G. T., Fan, X., Knapp, G. R., Schneider, D. P., Vanden Berk, D. E., Geballe, T. R., 2002. Unusual broad absorption line quasars from the sloan digital sky survey. *Astrophys. J. Suppl. Ser.* 141, 267–309.
- Hall, P. B., Hutsemékers, D., 2003. VLT Observations of two Unusual BAL Quasars. In: Collin, S., Combes, F., Shlosman, I. (Eds.), *Active Galactic Nuclei: From Central Engine to Host Galaxy.* p. 209.
- Hall, P. B., Hutsemékers, D., 2004. An MHD-driven Disk Wind Outflow in SDSS J0300+0048? In: Richards, G. T., Hall, P. B. (Eds.), *AGN Physics with the Sloan Digital Sky Survey.* p. 227.
- Hall, P. B., Hutsemékers, D., Anderson, S. F., Brinkmann, J., Fan, X., Schneider, D. P., York, D. G., Aug. 2003. VLT+UVES Spectroscopy of the Ca II Low-Ionization Broad Absorption Line Quasar SDSS J030000.56+004828.0. *Astrophys. J.* 593, 189–202.
- Hewett, P. C., Foltz, C. B., Apr. 2003. The Frequency and Radio Properties of Broad Absorption Line Quasars. *Astron. J.* 125, 1784–1794.
- Johansson, S., Zethson, T., Hartman, H., Ekberg, J. O., Ishibashi, K., Davidson, K., Gull, T., Sep. 2000. New forbidden and fluorescent Fe III lines identified in hst spectra of eta carinae. *Astron. Astrophys.* 361, 977–981.
- Knigge, C., Scaringi, S., Goad, M. R., Cottis, C. E., May 2008. The intrinsic fraction of broad-absorption line quasars. *Mon. Not. R. Astron. Soc.* 386, 1426–1435.
- Kochanek, C. S., Dai, X., Morgan, C., Morgan, N., Poindexter, G., S. C., Nov. 2007. Turning AGN Microlensing from a Curiosity into a Tool. In: G. J. Babu & E. D. Feigelson (Ed.), *Statistical Challenges in Modern Astronomy IV.* Vol. 371 of *Astronomical Society of the Pacific Conference Series.* p. 43.
- Korista, K., Baldwin, J., Ferland, G., Verner, D., Feb. 1997. An Atlas of Computed Equivalent Widths of Quasar Broad Emission Lines. *Astrophys. J. Suppl. Ser.* 108, 401–415.
- Kraft, R. P., Burrows, D. N., Nousek, J. A., Jun. 1991. Determination of confidence limits for experiments with low numbers of counts. *Astrophys. J.* 374, 344–355.

- Morris, S. L., Jul. 1988. The covering factor of quasar broad absorption line clouds. *Astrophys. J. Lett.* 330, L83–L86.
- Murray, N., Chiang, J., Grossman, S. A., Voit, G. M., Oct. 1995. Accretion disk winds from active galactic nuclei. *Astrophys. J.* 451, 498.
- Pen, U.-L., Jan. 1999. Analytical Fit to the Luminosity Distance for Flat Cosmologies with a Cosmological Constant. *Astrophys. J. Suppl. Ser.* 120, 49–50.
- Reichard, T. A., Richards, G. T., Hall, P. B., Schneider, D. P., Vanden Berk, D. E., Fan, X., York, D. G., Knapp, G. R., Brinkmann, J., Dec. 2003. Continuum and Emission-Line Properties of Broad Absorption Line Quasars. *Astron. J.* 126, 2594–2607.
- Shakura, N. I., Sunyaev, R. A., 1973. Black holes in binary systems. Observational appearance. *Astron. Astrophys.* 24, 337–355.
- Spergel, D. N., Bean, R., Doré, O., Nolta, M. R., Bennett, C. L., Dunkley, J., Hinshaw, G., Jarosik, N., Komatsu, E., Page, L., Peiris, H. V., Verde, L., Halpern, M., Hill, R. S., Kogut, A., Limon, M., Meyer, S. S., Odegard, N., Tucker, G. S., Weiland, J. L., Wollack, E., Wright, E. L., Jun. 2007. Three-Year Wilkinson Microwave Anisotropy Probe (WMAP) Observations: Implications for Cosmology. *Astrophys. J. Suppl. Ser.* 170, 377–408.
- Steenbrugge, K. C., Kaastra, J. S., Crenshaw, D. M., Kraemer, S. B., Arav, N., George, I. M., Liedahl, D. A., van der Meer, R. L. J., Paerels, F. B. S., Turner, T. J., Yaqoob, T., May 2005. Simultaneous X-ray and UV spectroscopy of the Seyfert galaxy NGC 5548. II. Physical conditions in the X-ray absorber. *Astron. Astrophys.* 434, 569–584.
- Steffen, A. T., Strateva, I., Brandt, W. N., Alexander, D. M., Koekemoer, A. M., Lehmer, B. D., Schneider, D. P., Vignali, C., Jun. 2006. The X-Ray-to-Optical Properties of Optically Selected Active Galaxies over Wide Luminosity and Redshift Ranges. *Astron. J.* 131, 2826–2842.
- Streblyanska, A., Barcons, X., Carrera, F. J., Gil-Merino, R., Feb. 2010. A revision of the X-ray absorption nature of the BALQSOs. [ArXiv:astro-ph/1002.0723](https://arxiv.org/abs/1002.0723).
- Surdej, J., Hutsemekers, D., May 1987. Geometry of the mass-outflows around broad absorption line QSOs and formation of the complex Ly-alpha + N V line profile. *Astron. Astrophys.* 177, 42–50.
- Trump, J. R., Hall, P. B., Reichard, T. A., Richards, G. T., Schneider, D. P., Vanden Berk, D. E., Knapp, G. R., Anderson, S. F., Fan, X., Brinkman, J., Kleinman, S. J., Nitta, A., Jul. 2006. A Catalog of Broad Absorption Line Quasars from the Sloan Digital Sky Survey Third Data Release. *Astrophys. J. Suppl. Ser.* 165, 1–18.
- Turnshek, D. A., 1986. Broad absorption line QSOs. In: Kapahi, V. K., Swarup, G. (Eds.), *Quasars*. Vol. 119 of IAU Symposium. pp. 317–328.
- Voit, G. M., Weymann, R. J., Korista, K. T., Aug. 1993. Low-ionization broad absorption lines in quasars. *Astrophys. J.* 413, 95–109.
- Weymann, R. J., Morris, S. L., Foltz, C. B., Hewett, P. C., May 1991. Comparisons of the emission-line and continuum properties of broad absorption line and normal quasi-stellar objects. *Astrophys. J.* 373, 23–53.

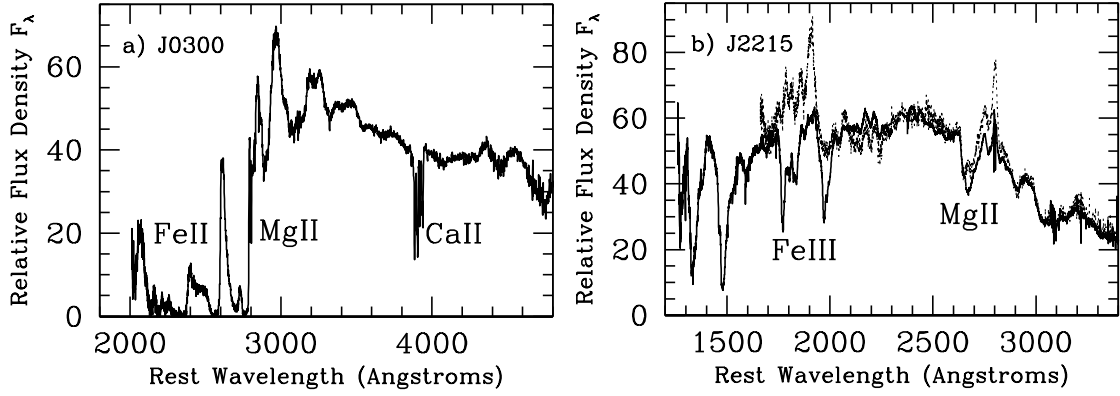


Figure 1: Spectra of the two target quasars, with selected absorption troughs marked. The vertical axes give F_λ in units of 10^{-17} erg s^{-1} cm^{-2} \AA^{-1} . **a.** The overlapping-trough object SDSS J0300+0048. Below 2800 \AA , Fe II and other troughs overlap to absorb nearly all the flux from the quasar. **b.** The Fe III-dominant BAL quasar SDSS J2215-0045 (solid) and a partial estimate of its intrinsic, unabsorbed spectrum (dashed), from Hall and Hutsemékers (2003). The UV34 and UV48 multiplets of Fe III are very strong in absorption, while only upper limits can be put on absorption from any Fe II multiplet.

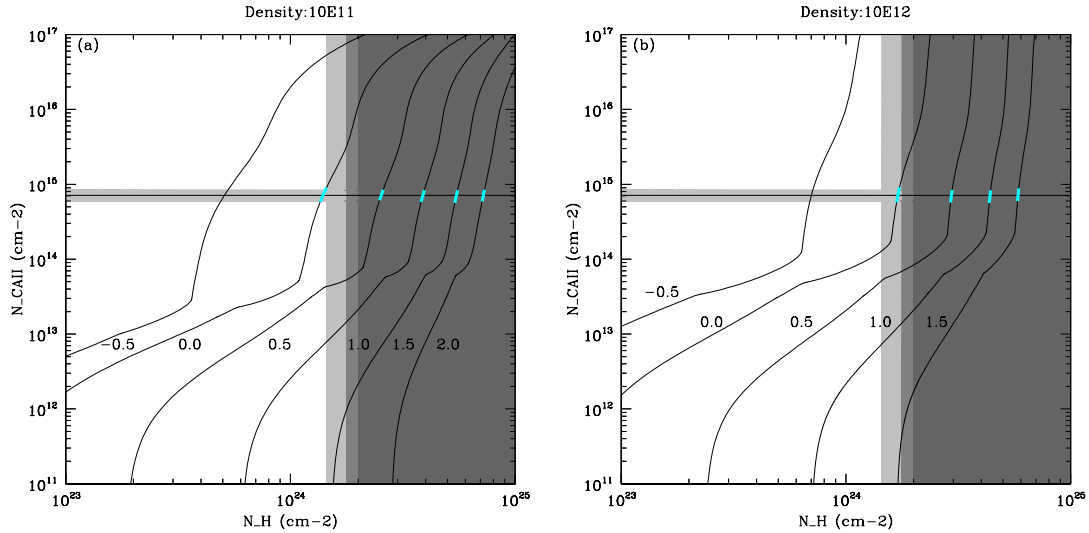


Figure 2: The behaviour of the Ca II column density for varying ionization parameter and density. Shaded regions represent constraints posed by column densities of Ca II and hydrogen in SDSS J0300+0048. The vertical lines separating the dark, light, and lightest shades of grey are the lower limits for the X-ray calculated hydrogen column density for the 90%, 95% and 99% confidence intervals, respectively. The light grey horizontal bar represents Ca II column density and its uncertainty. The log of the ionization parameter is labeled beside its corresponding curve. The cyan (black in hardcopy) highlights the regions for each ionization parameter where they are in the allowed parameter space. **(a)** Graph for $n_e = 10^{11}$ cm^{-3} . **(b)** Graph for $n_e = 10^{12}$ cm^{-3} . [A colour version of this figure is available in the online version]

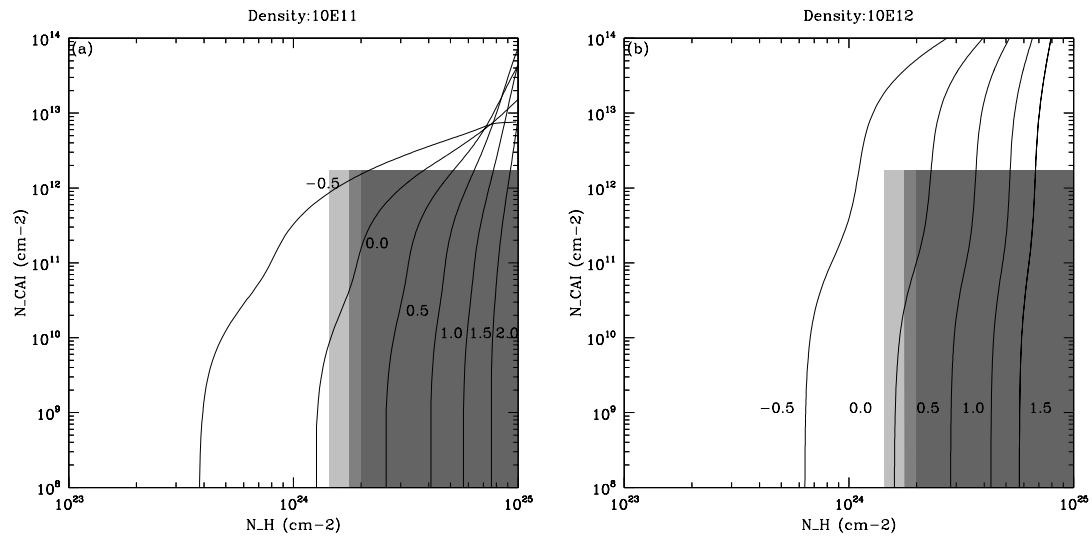


Figure 3: These curves correspond directly to the curves seen in Figure 2, as a check of how consistent the lower limit on the log of the ionization parameter is with other ions. A hard upper limit (calculated via UV spectroscopy) is set for the Ca I column density in SDSS J0300+0048. The same hydrogen column density is used for the vertically shaded regions. Again, the curves are labeled with their corresponding ionization parameter. **(a)** Graph for $n_e = 10^{11} \text{ cm}^{-3}$. **(b)** Graph for $n_e = 10^{12} \text{ cm}^{-3}$.

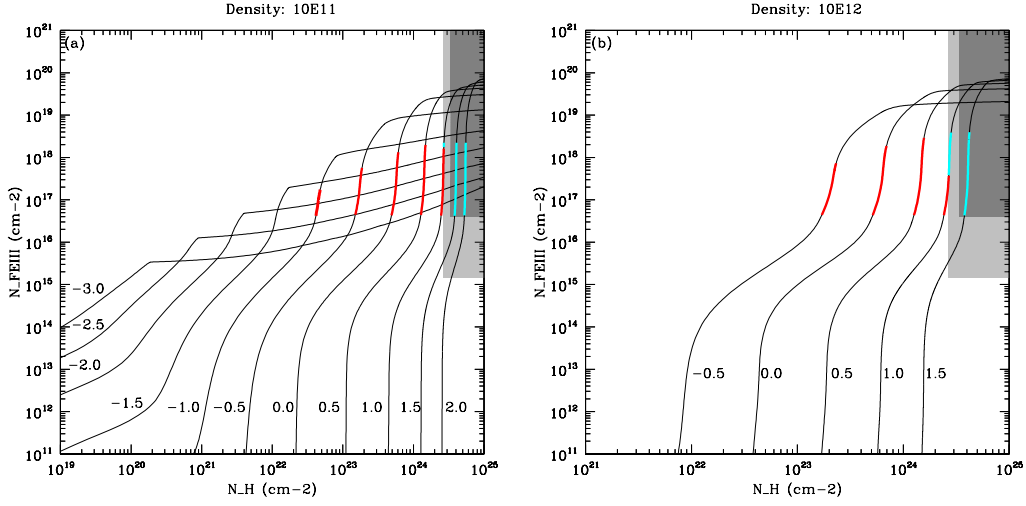


Figure 4: Curves represent the behaviour of the Fe III column density for varying ionization parameter and density. The lower limit on the hydrogen column in SDSS J2215–0045 is shown at 1σ (lightest grey) and 2σ (darker grey). An uncorrected (lightest grey) and corrected (darker grey) lower limit on the Fe III column is presented (see §5.2). The log of the ionization parameter is labeled beside its corresponding curve. The cyan (black in hardcopy) highlights denote the regions for which the curves satisfy both the lower limit Fe III column density and the lower limit hydrogen column density as well as the upper limit Fe II column density (see Figure 5). Red (light grey in hardcopy) highlights only satisfy the constraints posed by the Fe III and Fe II column densities, disregarding our lower limit on the hydrogen column. **(a)** Graph for $n_e = 10^{11} \text{ cm}^{-3}$. **(b)** Graph for $n_e = 10^{12} \text{ cm}^{-3}$. [A colour version of this figure is available in the online version]

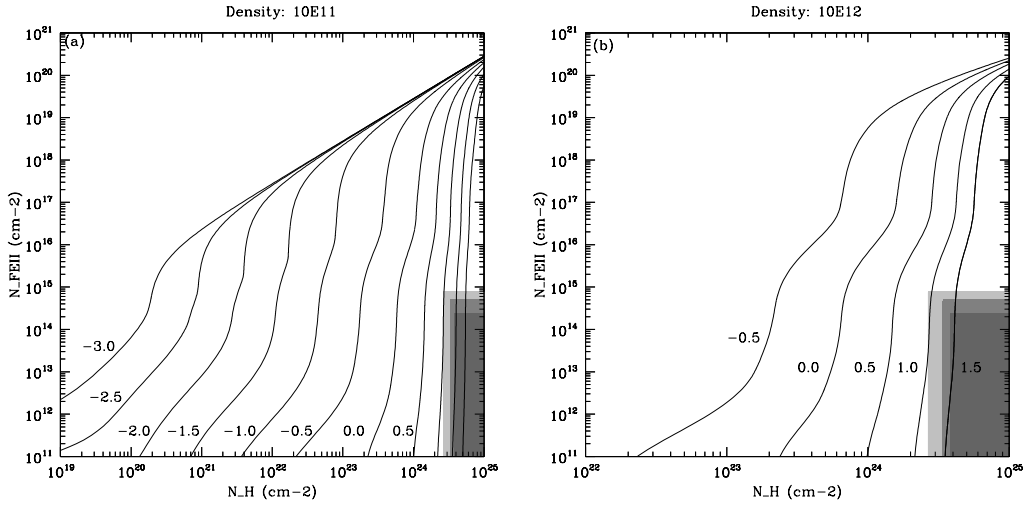


Figure 5: The relationship of Fe III and Fe II absorbing gas in this object is vital. Here we plot the same curves for each ionization parameter as seen in Figure 4, but in comparison to the upper limit on Fe II absorbing column (see § 5.2). The lower limit on the hydrogen column density is also the same as seen in Figure 4. These plots show that the ionization parameters supported by the lower limit on the Fe III column are also supported by the upper limit on the Fe II column density. **(a)** Graph for $n_e = 10^{11} \text{ cm}^{-3}$. **(b)** Graph for $n_e = 10^{12} \text{ cm}^{-3}$.

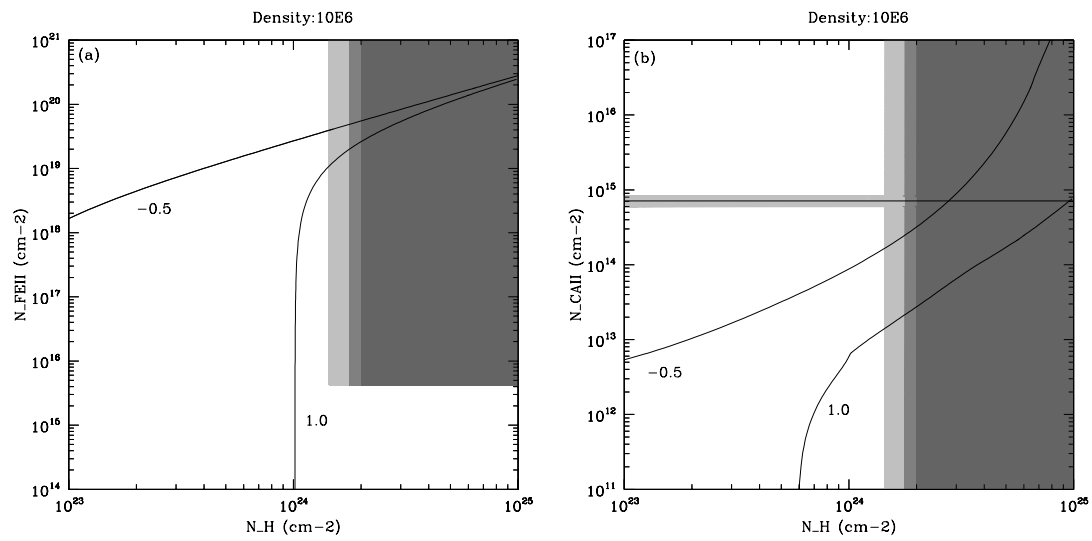


Figure 6: Two CLOUDY runs for $\log U = -0.5, 1.0$ and $n_e = 10^6 \text{ cm}^{-3}$. The curves representing each ionization parameter are labeled. The shaded areas represent the allowed column densities of (a) Fe II and (b) Ca II in SDSS J0300+0048 based on UV observed column density limits and the lower limit, X-ray derived hydrogen column.

Appendix A. Fe III Column Density Lower Limits for SDSS J2215–0045

The lower limit for the Fe III column density in SDSS J2215–0045 was calculated (after normalizing by the unabsorbed continuum shown in Figure 1b) using absorption from Fe III ions in the lower levels of the UV34 and UV48 triplets (3.73 and 5.08 eV above ground, respectively). The individual components of each triplet are severely blended. Therefore, we treat each triplet’s trough as coming from a single line with a λf value equal to the average of the components of the triplet, and then divide the resulting column density by three. We assume that the covering factor of the line is unity, so that the optical depth τ_ν at each velocity ν is given by $\tau_\nu = -\log I_\nu$, where I_ν is the absorbed continuum at ν normalized by the assumed unabsorbed continuum at ν . The resulting τ_ν is always optically thin ($\tau_\nu \lesssim 0.6$). We find a raw lower limit of $\log N_{\text{FeIII}} > 15.18$ (lightest grey region in Figure 4). Even this is the largest Fe III column observed in any outflow to date and is nearly ten times the N_{FeIII} observed in FBQS 0840+3633 by de Kool et al. (2002).

We can set an improved $\log N_{\text{FeIII}}$ lower limit by attempting to account for Fe III ions in other levels. Assuming unsaturated troughs and that the excited Fe III level populations follow a Boltzmann distribution, the relative number densities in the two observed states yield $T_{\text{ex}} = 34,250$ K. Accounting for Fe III ions in all levels with excitation energy ≤ 5.08 eV at that temperature yields a factor of 28 correction from observed to total column in Fe III. Thus the lower limit we adopt is $\log N_{\text{FeIII}} > 16.62$ (darker grey region in Figure 4).

It is important to note that the true Fe III column density could be substantially higher than any of the above estimates if the troughs are saturated, which is quite likely (Hall and Hutsemékers 2003). For example, M. Bautista (personal communication) finds a maximum possible ratio of $N_{\text{UV48}}/N_{\text{UV34}} = 0.158$ at $n_e > 10^{9.5} \text{ cm}^{-3}$, whereas we observe a value of 0.447 assuming unsaturated troughs. If we conservatively assume that only the UV48 trough is unsaturated and use the maximum possible value of $N_{\text{UV48}}/N_{\text{FeIII}} = 0.00155$, again found at $n_e > 10^{9.5} \text{ cm}^{-3}$ (M. Bautista, personal communication), we obtain $\log N_{\text{FeIII}} > 17.49$. Note that a density $n_e = 10^{7.5} \text{ cm}^{-3}$ would imply $\log N_{\text{FeIII}} = 18.5$ and a density $n_e = 10^{6.5} \text{ cm}^{-3}$ would imply $\log N_{\text{FeIII}} = 19.5$.